ACS APPLIED ENERGY MATERIALS

www.acsaem.org Article

Enhanced Efficiency and Stability of Planar Perovskite Solar Cells Using a Dual Electron Transport Layer of Gold Nanoparticles Embedded in Anatase TiO_2 Films

Da-Wei Zhao,[‖] Ming-Yu Yu,[‖] Ling-Ling Zheng,[‖] Ming Li, Shi-Jie Dai, Di-Chun Chen, Tung-Chun Lee,* and Da-Qin Yun*

Cite This: *ACS Appl. Energy Mater.* 2020, 3, 9568−9575 Read Online

ACCESS | Metrics & More | Article Recommendations | Supporting Information

ABSTRACT: Incorporating plasmonic nanostructures is a promising strategy to enhance both the optical and electrical characteristics of photovoltaic devices via more efficient harvesting of incident light. Herein, we report a facile fabrication scheme at low temperature for producing gold nanoparticles embedded in anatase TiO_2 films, which can simultaneously improve the efficiency and stability of n−i−p planar heterojunction perovskite solar cells (PSCs). The PSCs based on rigid and flexible substrates with 0.2 wt % Au−TiO_2/TiO_2 dual electron transport layers (ETLs) achieved power conversion efficiencies up to 20.31 and 15.36%, superior to that of devices with TiO_2 as a single ETL. Moreover, 0.2 wt % Au−TiO_2/TiO_2 devices demonstrated significant stability in light soaking, which is attributed to improved light absorption, low charge recombination loss, and enhanced carrier transport, and extraction with the plasmonic Au−TiO_2/TiO_2 dual ETL. The present work improves the practicability of high-performance and flexible PSCs by engineering the photogenerated carrier dynamics at the interface.

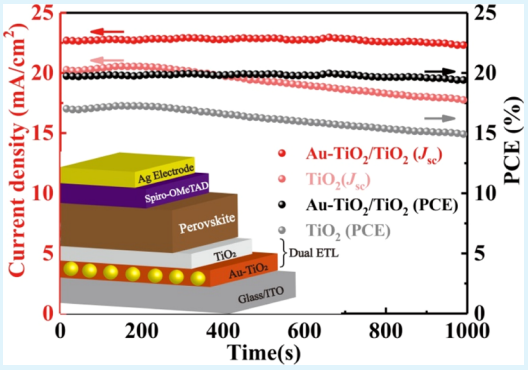

KEYWORDS: *perovskite solar cell, electron selective layer, low-temperature solution process, plasmonic nanostructure, flexible solar cell*

1. INTRODUCTION

Perovskite solar cell (PSC) is one of the key technologies in developing modern electronic devices because of its high power conversion efficiency (PCE > 25%), good flexibility, affordable costs, simple solution-based fabrication process, and potential application for scalable products.[1,2] However, so far, the poor long-term stability of PSC still hinders its commercialization.[3,4] The instability issues of PSC are mainly due to the low chemical stability of organic−inorganic hybrid perovskite materials upon exposure to external environments, such as moisture, oxygen, temperature, light soaking, and electrical biasing.[5,6] In this context, various methods have been developed to address these problems.[7−9] Interface modification has been proven to enable PSC working more stable and more efficiently. Perovskite crystal growth can be controlled to tune the film morphology for regulating ion migration and the density of trap states, resulting in a reduction in carrier recombination and the charge transfer/extraction barrier.[10−12] In particular, a significant amount of effort has been focused on reducing ions transportation in the perovskite layers,[13−15] modifying the electron and hole selective layers,[16−18] as well as blocking the reactions between metal electrodes and halides.[19]

Compared to the conventional methods, incorporating plasmonic nanostructures, as a novel interfacial tailoring technique, has been proven to enhance the PCE of PSCs more efficiently because it possesses broadly tunable optical properties coupled with photovoltaic active surfaces that simultaneously benefit photon energy and electron management.[20−22] Moreover, it is noteworthy that gold nanoparticles (Au NPs) exhibit both high thermal stability and high chemical stability, as well as localized surface plasmon resonance (LSPR) in the visible-to-near-infrared (vis-NIR) range. The resulted near- and far-optical field effects can produce intense absorption, scattering, and significantly enhanced electromagnetic (EM) fields in the nanoscale vicinity of their surface, which have a sensitive dependence on the size, shape, and dielectric environments of NPs.[23] It can be seen that the dielectric environment of Au NPs plays an essential role in optimizing the EM field distribution of LSPR, which will further influence the charge carrier dynamics and free carrier absorption in photovoltaic materials.[24] For instance, in 2013,

Received: February 9, 2020
Accepted: September 14, 2020
Published: September 14, 2020

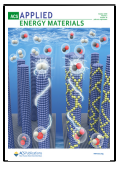

https://dx.doi.org/10.1021/acsaem.0c00276
ACS Appl. Energy Mater. 2020, 3, 9568−9575

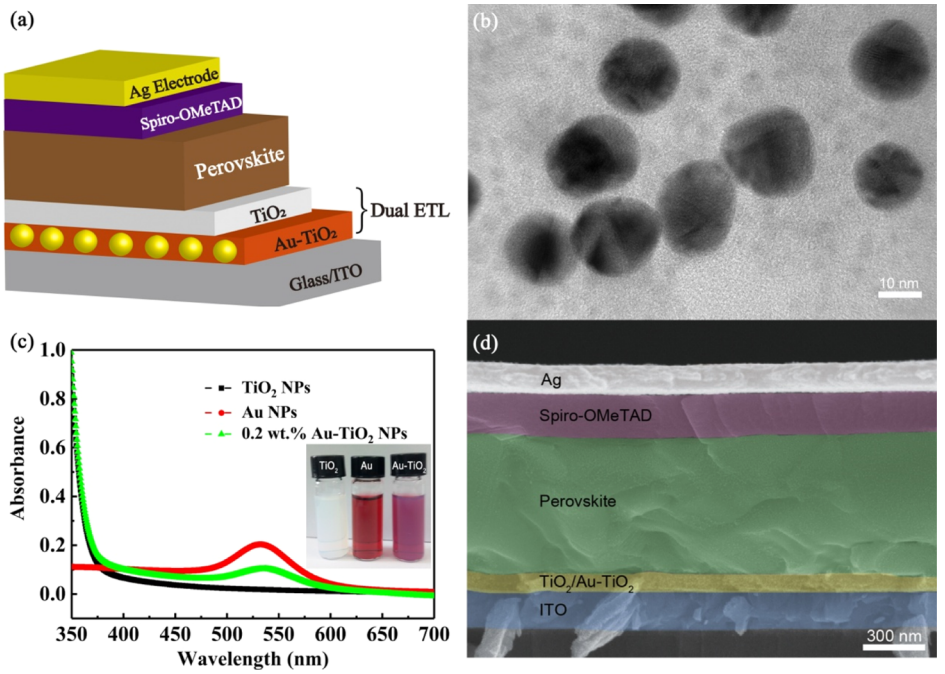

Figure 1. (a) Schematic diagram showing the device configuration. (b) TEM image of 0.2 wt % Au−TiO_2 NPs. (c) Absorption of TiO_2 NPs, Au NPs, and 0.2 wt % Au−TiO_2 NPs composite solutions with inset showing the photographs of the three solutions. (d) Cross-sectional SEM image of the internal structure in the PSC.

Snaith reported for the first time the introduction of Au@SiO_2 core−shell NPs into an Al_2O_3 matrix. Such a modified electron transport layer (ETL) succeeded in improving the performance of PSCs by plasmonic effects. The improvement was caused by a decrease in the exciton binding energy of perovskite materials; however, the light absorption was not increased.[25] Subsequently, these features have been extensively studied by the introduction of various dielectric coatings into PSC configurations, such as SiO_2,[26,27] TiO_2,[28−30] and MgO,[31] in which Au NPs have been interfaced with TiO_2 to maximize the charge separation of hot electrons.[24,32] Although these plasmonic nanostructures have demonstrated some promise in the efficiency enhancement of PSCs by plasmonic effects, there is rare research in investigating the low-temperature solution-processed plasmonic nanostructures of the Au NPs embedded in anatase TiO_2 films, especially for their application in flexible PSCs.

Herein, we apply facile interface engineering to create plasmonic nanostructures of Au NPs embedded in anatase TiO_2 layers, where the Au NPs and the anatase TiO_2 NPs are prepared in aqueous media and the Au−TiO_2/TiO_2 dual ETLs are directly deposited from aqueous solutions containing various weight ratios of Au NPs and TiO_2 NPs. Based on the n−i−p structure of ITO/0.2 wt %Au−TiO_2/TiO_2/$(HC(NH_2)_2PbI_3)_x(CH_3NH_3PbCl_3)_{1-x}$/spiro-OMeTAD/Ag, the photovoltaic performance of PSCs can be rationalized by optimizing the physical properties of the ETL and the interface between the ETL and perovskite layer. With the help of Au NPs, the highest PCE of the PSCs on rigid and flexible substrates can reach 20.31 and 15.36%, respectively, superior to that of devices with TiO_2 as a single ETL (champion PCE = 17.19% on a rigid substrate and champion PCE = 12.80% on a flexible substrate). Moreover, the devices based on plasmonic nanostructures demonstrate improved stability in light soaking compared to those using a pure TiO_2 film as an ETL, which is attributed to the higher light absorption efficiency, improved interface charge transfer rate, and reduced recombination loss, as supported by our stable external quantum efficiency (EQE), the significant fluorescence quenching in photoluminescence (PL) measurements and electrochemical impedance spectroscopy (EIS) data.

2. EXPERIMENTAL SECTION

2.1. Materials and Synthesis. TiO_2 NPs were synthesized from the sol−gel way according to the previous research.[33] Titanium(IV) isopropoxide was dropped into deionized water mixed with nitric acid accompanied with intense stirring. Then after hydrolysis, it formed a white TiO_2 NPs colloid; the colloid was heated to 80 °C meanwhile stirred intensely, to produce the TiO_2 NPs (20 mg mL^{-1}). Last, the TiO_2 NPs needed to be filtered using a 0.45 μm polyvinylidene fluoride syringe filter.

Au NPs were synthesized according to the procedures described in the literature.[34] $HAuCl_4{\cdot}3H_2O$ (99.9%) and sodium citrate dihydrate (99%) were both purchased from Sigma-Aldrich. Typically, 1 mL of 60 mM sodium citrate and 1 mL of a 25 mM $HAuCl_4$ solution were sequentially injected into 50 mL of a vigorously boiling 2.2 mM sodium citrate aqueous solution. Boiled this mixture for 15 min and then continued stirring for another 15 min. The yielded Au seed solution needed to be cooled down to 90 °C. After that, 1 mL of sodium citrate (60 mM) and 1 mL of a $HAuCl_4$ solution (25 mM) were injected sequentially. The reaction lasted for about 30 min. By repeating this operation (sequential injection of 1 mL of 60 mM sodium citrate and 1 mL of 25 mM $HAuCl_4$), the sizes of Au NPs grew progressively, cooled the resulting Au NPs solution to room temperature, filtered then stored it under 4 °C.

2.2. Fabrication. Before being used, ITO required ultrasonic cleaning. The Au−TiO_2 NPs solution was prepared by adding different amounts of Au NPs into the as-synthesized TiO_2 NPs solution at the loading ratio from 0.1 to 0.3 wt %. The Au−TiO_2 NPs and TiO_2 NPs solutions (20 mg mL^{-1} for both solutions) were sequentially coated by spinning at 4000 rpm for 40 s, afterward, annealed at 150 °C for 1 h. To form a perovskite film, the preparation method for PbI_2 [dimethylsulfoxide (DMSO)] complex based on a

https://dx.doi.org/10.1021/acsaem.0c00276
ACS Appl. Energy Mater. 2020, 3, 9568−9575

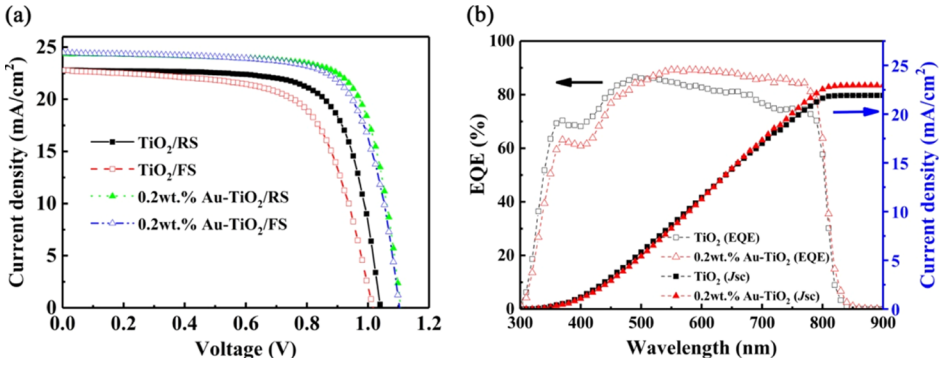

Figure 2. (a) Champion $J-V$ curves and (b) EQE plots of the PSCs.

previous report was applied.[35] Formamidinium iodide (FAI) and methylamine chloride (MACl) were prepared in a typical way according to former research.[36] The 1.5 M PbI_2 (DMSO) complex dissolved in DMF was coated by spinning at 2500 rpm for 40 s. Subsequently, spin-coated the FAI/MACl mixture (70 mg mL^{-1}) with 2500 rpm for 40 s. Then, annealed at 120 °C. Cooling down to room temperature, then deposited spiro-OMeTAD at 2000 rpm for 40 s to form a hole transport layer. The spiro-OMeTAD solution was made by dissolving spiro-OMeTAD into chlorobenzene (60 mM) with 30 mM Li-TFSI (520 mg mL^{-1} in acetonitrile), 200 mM 4-tBP, and 1.8 mM FK209 (300 mg mL^{-1} in acetonitrile). Eventually, a 100 nm of silver electrode with an active area of 0.1 cm^2 was made through thermal evaporation with the help of a mask to pattern the electrode. To fabricate flexible PSCs, the only different thing was to use patterned ITO-PEN substrates with a 0.06 cm^2 active area.

2.3. Characterization. The structure and morphology were explored by transmission electron microscopy (TEM, JEOL JEM2100) and field-emission scanning electron microscopy (SEM, ZEISS SUPRA 55). The absorbance spectra were tested using an ultraviolet−visible spectrophotometer (UV−vis, UV-2600). Electrical properties of the Au−TiO_2 and TiO_2 layers were evaluated by the PL (F-7000) and time-resolved PL (TRPL, FLS-980) spectra. The current density−voltage ($J-V$) curves were tested by the Keithley 2400 source meter under 1 sun illumination (AM 1.5 G, 100 mW cm^{-2}). Unless otherwise noted, the devices were tested in the forward and reverse scan with a 20 ms dwell time. The hysteresis index was calculated according to a previously reported formula to quantify the hysteresis effect of PSCs.[37] The external quantum efficiency (EQE) spectra was tested via the EQE system (Newport). The EIS was tested via the VersaSTAT 3. The stabilized-efficiency measurement was tested via the CHI660E.

3. RESULTS AND DISCUSSION

3.1. Composition and Structure. We prepared Au NPs via a low-temperature fabrication scheme and embedded them into TiO_2 films to make Au−TiO_2 films function as ETLs. The TiO_2 film is composed of nanocrystalline anatase TiO_2 NPs prepared using a low-temperature solution-based approach developed by us previously.[34] Their small and uniform particle morphology facilitates the incorporation of Au NPs within the ETL matrix and allow fine control over the ETL thickness.

To maximize the LSPR effect of Au NPs and thus to maximize the light-harvesting ability of the active layer, the Au NPs should be close to or dispersed well into the perovskite layer. However, the perovskite film in immediate contact with the metallic nanoparticles will lead to rapid charge recombination and excitons quenching.[38] Thus, in order to avoid the adverse effects, the n−i−p PSCs were composed of ITO/Au−TiO_2/TiO_2/$(FAPbI_3)_x(MAPbCl_3)_{1-x}$/spiro-OMeTAD/Ag in this work (Figure 1a). In particular, a dual ETL of Au−TiO_2/TiO_2 was employed and optimized to minimize energy losses, while maximizing the plasmonic effects on both the ETL and the perovskite layer.

A schematic of plasmon-induced charge transport was provided to understand the impact of Au NPs on the PSCs in detail, as shown in Figure S1. On one hand, the far-field effect of Au NPs acts as the scattering substance can increase the light travel distance in perovskite, which can effectively improve the absorption of photons of the active layer; on the other hand, the near-field effect can facilitate more hot electrons into the conduction band of ETL, thereby enhancing the charge transport and collection of pure TiO_2.

Also, the electrical conductivity of different ETLs (Figure S2) is studied according to the methods reported in the previous literature.[39,40] The active area and thickness of all samples will be the same, so we can determine the electrical conductance of each ETL from the $I-V$ curve slope. The conductivity of ETLs rises progressively with the content of the metallic Au NPs, which implies that Au−TiO_2 ETLs have stronger charge transport capability.

The morphologies of the as-prepared Au NPs and 0.2 wt % Au−TiO_2 NPs are shown in Figures S3 and 1b, respectively. The Au NPs (16 ± 2 nm) are uniformly dispersed and embedded into the TiO_2 matrix. The selected area electron diffraction pattern (Figure S3, inset) shows typical electron diffraction rings corresponding to the (111), (200), (220), and (311) lattice planes of the crystal structure of Au, consistent to the reported results.[41] Figure 1c and the inset show typical sample solutions of TiO_2 NPs, Au NPs, and the 0.2 wt % Au−TiO_2 NPs in water, as well as their corresponding UV−vis extinction spectra. Both the Au NPs and the 0.2 wt % Au−TiO_2 NPs exhibit a deep red color with a maximum absorption peak at 527 nm owing to the LSPR property of the Au NPs.[23] The UV−vis transmittance spectra of different ETLs is shown in Figure S4; however, the 0.2 wt % Au−TiO_2 NPs thin film hardly changed in transmittance between 400 and 800 nm. The result shows that the introduction of Au NPs causes only a slight decrease of transmittance in the ultraviolet region.

Indeed, the photovoltaic device characteristics is strongly dependent on perovskite film properties. A desirable $(FAPbI_3)_x(MAPbCl_3)_{1-x}$ perovskite layer displayed in the SEM image exhibited compact and highly crystalline morphology, which can facilitate charge transfer and inhibit grain−boundary charge recombination.

3.2. Rigid Devices. To investigate the effects of incorporating Au NPs within the ETL, we prepared the ETLs containing various weight ratios of Au−TiO_2 (0, 0.1, 0.2, and 0.3 wt %), see Figure S5 for the measured $J-V$ curves and Table S1 for photovoltaic parameters. According to the

https://dx.doi.org/10.1021/acsaem.0c00276
ACS Appl. Energy Mater. 2020, 3, 9568−9575

Table 1. Photovoltaic Parameters

ETL	substrate	scanning direction[a]	V_{OC} [V]	J_{SC} [mA cm^{-2}]	FF [%]	PCE [%]	hysteresis index
TiO_2	ITO-glass	F (champion)	1.02	22.81	65.68	15.23	0.11
	ITO-glass	R (champion)	1.04	22.79	72.52	17.19	
0.2 wt % Au−TiO_2/TiO_2	ITO-glass	F (champion)	1.10	24.49	72.67	19.62	0.03
	ITO-glass	R (champion)	1.11	24.36	75.33	20.31	

[a]R indicates reverse scanning directions.

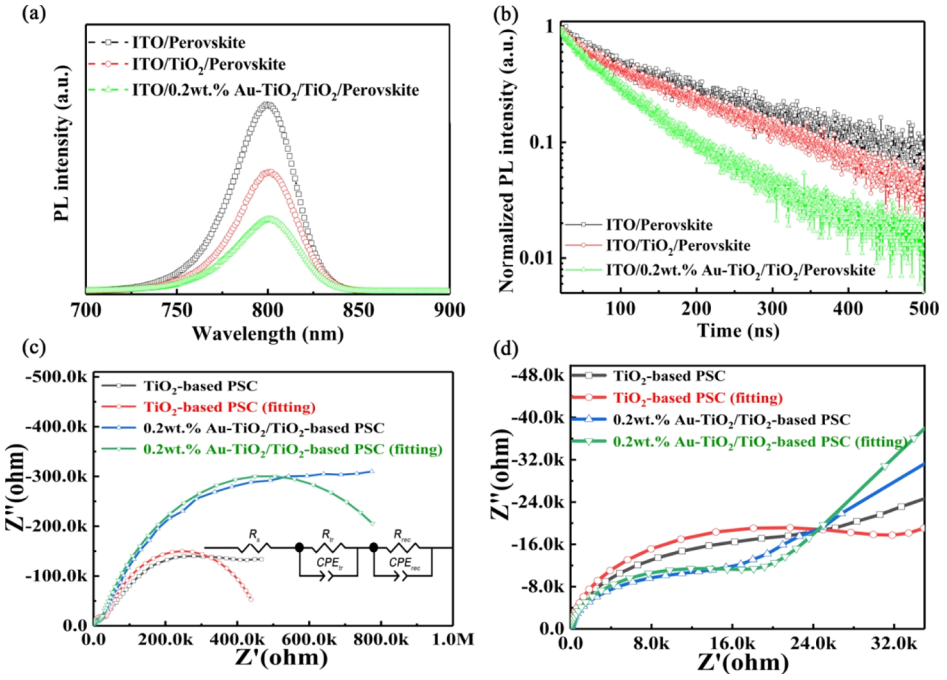

Figure 3. (a) Steady-state and (b) TRPL spectra. (c) Nyquist plots with inset showing the equivalent circuit model for the PSCs in EIS. (d) Magnification of the high-frequency region of Nyquist plots of PSCs.

statistical results (Figure S7) from 20 identical Au−TiO_2/TiO_2-based devices, when the concentration of Au NPs increased from 0 to 0.2 wt % Au−TiO_2, the PSC devices showed an increase in the PCE, which may have resulted from the multifunctional Au NPs in anatase TiO_2 via enhancing the photocurrent and improve the electrical properties of pure TiO_2. However, as the concentration continued to increase, the PCE began to decrease. Such a decline may be attributed to excess recombination centers provided by the excess Au NPs. Here, the optimal concentration of Au NPs in anatase TiO_2 was found to be approximately 0.2 wt %. Interestingly, the device based on a single Au−TiO_2 ETL without the TiO_2 top layer exhibits much lower V_{OC} and FF than that of the pure TiO_2 ETL as well as that of Au−TiO_2/TiO_2 dual ETL, resulting in the lowest PCE (Figure S6 and Table S2). This may be caused by Au NPs embedded in the TiO_2 layer that act as charge traps once in direct contact with the perovskite film, leading to an increased rate of interfacial carrier recombination,[28,31] compared to the Au−TiO_2/TiO_2 dual ETL.

Figure 2a and Table 1 show the J−V curves and detailed parameters of the rigid PSCs based on the TiO_2 ETL and 0.2 wt % Au−TiO_2/TiO_2 ETL. In particular, the rigid 0.2 wt % Au−TiO_2/TiO_2 PSCs exhibit considerably low hysteresis indices (0.03) and show a J_{SC} of 24.36 mA cm^{-1}, a V_{OC} of 1.11 V, and an FF of 75.33%, corresponding to a high PCE of 20.31%, which shows a significant improvement over that of the control device (hysteresis index = 0.11, PCE = 17.19%) using a single TiO_2 film as the ETL. The increased PCE and suppressed hysteresis could be due to the plasmonic effects of Au NPs on the TiO_2 ETL, which can promote electrons to transfer into TiO_2, leading to an enhancement in the improvement of V_{OC}, J_{SC}, and FF.[42]

To further confirm the improvement of the light-harvesting ability of the devices with Au NPs, EQE spectra was measured and is shown in Figure 2b. It can be clearly observed that the EQE of the sample with 0.2 wt % Au−TiO_2/TiO_2 ETL has an enhancement in (492−850 nm range) but a small reduction in (350−492 nm range) regions compared to that of the TiO_2 ETL, as shown in Figure 2b. These results may be due to the far field effect that improves the perovskite absorbance in the visible region, and to the near field effect that decreases the TiO_2 transmittance, leading to a light reduction reaching the perovskite in the UV region.[43] The integrated J_{SC} of the PSCs generated from the EQE were 21.92 and 22.95 mA cm^{-2} for TiO_2 and 0.2 wt % Au−TiO_2/TiO_2, respectively. These results indicate that PSCs with 0.2 wt % Au−TiO_2/TiO_2 ETLs indeed exhibit a plasmonic effect, resulting in increasing the photocurrent. However, LSPR may not be sufficient to explain all improvements in the photovoltaic parameters of the devices. The increase in the EQE in the wavelength range 492−850 nm can also be partially resulted from enhanced electrical properties in the presence of Au NPs.

3.3. Morphological, Optical, and Electrical Behaviors.

The morphology of the substrate may affect the quality of the

https://dx.doi.org/10.1021/acsaem.0c00276
ACS Appl. Energy Mater. 2020, 3, 9568−9575

Table 2. Biexponential Decay Dynamics

sample	τ_1 (ns)	f_1 (%)	τ_2 (ns)	f_2 (%)	τ_{ave} (ns)
ITO/perovskite	34.89	6.83	208.10	93.17	196.27
ITO/TiO_2/perovskite	28.69	7.07	193.70	92.93	182.03
ITO/0.2 wt % Au−TiO_2/TiO_2/perovskite	37.18	19.26	98.07	80.74	86.34

Table 3. Fitted Data from the EIS Measurements

ETL	R_s (Ω)	R_{tr} (Ω)	R_{rec} (Ω)	C_{tr} (F)	C_{rec} (F)
TiO_2	1.688	3.009×10^4	4.367×10^5	9.597×10^{-9}	4.746×10^{-7}
0.2 wt % Au−TiO_2/TiO_2	1.542	1.645×10^4	9.266×10^5	9.374×10^{-9}	5.111×10^{-7}

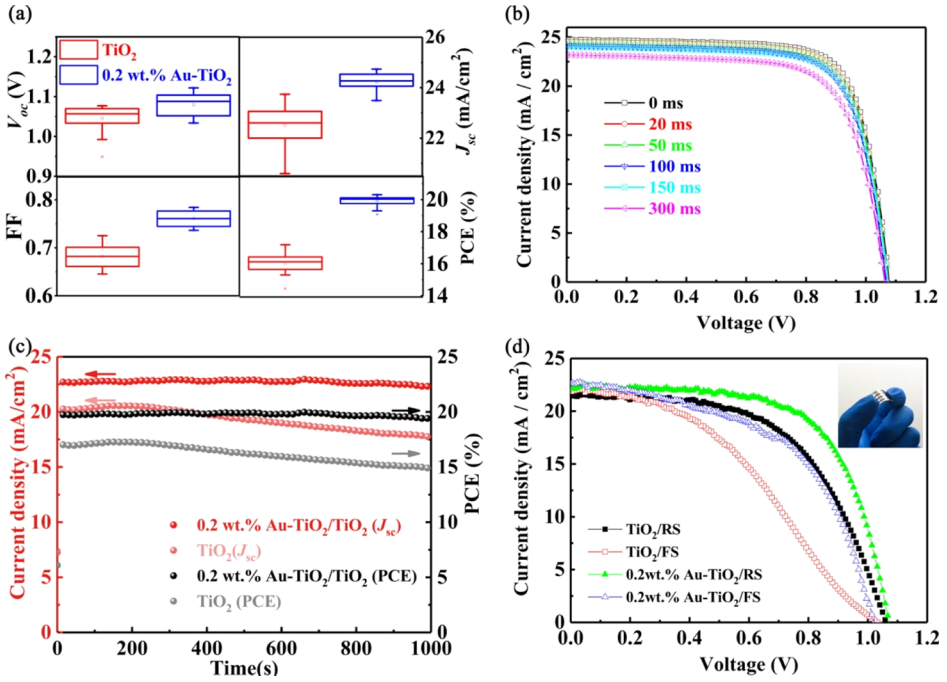

Figure 4. (a) Statistical deviation of the photovoltaic parameters. (b) $J-V$ curves of the PSCs based on 0.2 wt % Au−TiO_2/TiO_2 ETLs conducted at different dwell times. (c) Stabilized-efficiency measured at 0.84 and 0.87 V bias, respectively. (d) $J-V$ curves of the flexible PSCs and the inset shows the prototype of a flexible PSC.

perovskite, so we explored the SEM morphology of different substrates and perovskites based on different substrates, as shown in Figure S8. It can be seen from the figure that the surface morphology of different substrates is very smooth and dense, and there is almost no obvious difference. In addition, the overall perovskite grain size is very uniform, and the perovskite crystals have similar quality.

To obtain insights into the interfacial dynamics of the charge extraction at the ETL/perovskite, we obtained steady-state PL spectra and UV−vis spectra as shown in Figures 3a and S9, respectively. Although the device based on Au−TiO_2 does not show an obvious advantage in the absorption coefficient over the device based on pure TiO_2 because the absorption coefficient of the perovskite is much higher than that of Au NPs,[44] the increase in the photocurrent generation and the reduction in recombination loss could be further confirmed by PL measurements. The intensity of an emission peak centered at ~800 nm (Figure 3a), is reduced to nearly one-third via the insertion of the TiO_2 ETL. Further fluorescence quenching for the ITO/0.2 wt % Au−TiO_2/TiO_2/perovskite sample indicates that the metallic Au NPs modification is beneficial to interfacial charge extraction.

To further study the recombination rate of different devices, TRPL decay spectra is shown in Figure 3b. It is worth noting that the significant fluorescence quenching for the ITO/0.2 wt % Au−TiO_2/TiO_2/perovskite sample is likely caused by the increase in electrical conductance of the ETL and more efficient charge extraction provided by the metallic Au NPs. Compared to those of the ITO/perovskite (196.27 ns) and the ITO/TiO_2/perovskite (182.03 ns), PL quenching of the ITO/0.2 wt % Au−TiO_2/TiO_2/perovskite sample exhibits the fastest decay time of 86.34 ns (Table 2), which implies that radiative electron−hole recombination is suppressed and hence improves the performance of the devices via the enhanced light harvesting capability.

In addition to optical characterization, EIS measurements were performed in a dark environment to investigate the interfacial electrical dynamics. Figure 3c shows the Nyquist plots for the PSCs based on TiO_2 and Au−TiO_2/TiO_2 tested at a voltage bias of 0.4 V. Typically, in the Nyquist plot, the high frequency arc is controlled by charge transport kinetics, while the low frequency arc is controlled by charge recombination processes.[45] For a clearer view, Figure 3d shows the zoom-in of the high-frequency region. The fitted equivalent circuit model (inset of Figure 3c) mainly contains

https://dx.doi.org/10.1021/acsaem.0c00276
ACS Appl. Energy Mater. 2020, 3, 9568−9575

three electrical components: series resistance (R_s), transport (R_{tr}) in parallel with the constant phase angle element (CPE_{tr}), and recombination (R_{rec}) parallel in parallel with another element (CPE_{rec}).[46] R_{tr} and R_{rec} are typically related to the high-frequency arc and the low-frequency arc, respectively. As shown in Table 3, the R_s value of the PSC based on 0.2 wt % Au−TiO_2/TiO_2 is slightly lower than the pristine TiO_2-based PSC. Compared to the control device, the R_{tr} and R_{rec} values of the PSC based on 0.2 wt % Au−TiO_2/TiO_2 are reduced by 45% and enhanced by 112%, indicating that the Au−TiO_2 interlayer decreases charge recombination loss.

3.4. Stability of Devices. We prepared a series of cells under the same conditions to test the stability and reproducibility of the PSCs. Statistical data based on 20 cells illustrates the reproducibility and uniformity of the PSC performance, as shown in Figure 4a. The J−V curves of the Au−TiO_2/TiO_2-based PSCs exhibit excellent stability of current hysteresis over a wide range of dwell time (0−300 ms), as shown in Figure 4b. Also, the stabilized photocurrent was measured at a constant bias of 0.84 and 0.87 V, respectively, to test the light-soaking stability of devices. As shown in Figure 4c, a maximal steady-state J_{SC} of the TiO_2-based and 0.2 wt % Au−TiO_2-based PSCs is 20.51 and 22.93 mA cm^{-2}, with a corresponding PCE of 17.23 and 19.95%, respectively. Additionally, devices based on 0.2 wt % Au−TiO_2/TiO_2 ETL remains stable during the period of 1000 s. These results indicate that the 0.2 wt % Au−TiO_2/TiO_2 ETL contributes to the enhanced device light-soaking stability. The enhancement of photovoltaic performance and device light-soaking stability rely on multiple factors, including efficient interfacial charge transport, low charge recombination loss, and the additional photocurrent due to LSPR-induced direct transfer of hot electrons,[44] all of which can attribute to effects of the Au−TiO_2 interface layer.

3.5. Flexible Devices. Our low-temperature solution-based approach allows the 0.2 wt % Au−TiO_2/TiO_2 ETL to be fabricated on mechanically flexible ITO/PEN substrates. Figure 4d shows the champion J−V curves of the flexible devices. The flexible 0.2 wt % Au−TiO_2/TiO_2 PSCs exhibit considerably low hysteresis indices (0.19) while showing a PCE of 15.36%, which shows a significant improvement compared to the control device (hysteresis index = 0.31, PCE = 12.80%), as shown in Table S3. Detailed photovoltaic parameters of 10 flexible devices are shown in Figure S10, indicating reproducible enhancement in the performance of flexible PSCs via the incorporation of Au NPs into the TiO_2 layers, as discussed above. The inset of Figure 4d shows a prototype of flexible PSCs bending freely.

4. CONCLUSIONS

In conclusion, we have developed a dual ETL with embedded plasmonic nanostructures for rigid and flexible PSCs with high efficiency achieved. Such a dual ETL is fabricated via a low-temperature solution-processed approach. The bottom is a hybrid layer consisting of plasmonic Au NPs embedded in anatase TiO_2 films, while the top layer is purely made of nanocrystalline anatase TiO_2 NPs, which is indispensable in preventing a direct contact between Au NPs and the perovskite. The optimized 0.2 wt % Au−TiO_2 layer greatly benefited the ETL/perovskite interface by stimulating interfacial charge transfer, improving light absorption and inhibiting interfacial charge recombination. Thus, the champion PCEs of PSCs based on 0.2 wt %Au−TiO_2/TiO_2 ETLs were 20.31 and 15.36% on rigid and flexible substrates, respectively. This research provides a facile route for the design of flexible PSCs with high performance in a scalable fashion.

■ ASSOCIATED CONTENT

Supporting Information

The Supporting Information is available free of charge at https://pubs.acs.org/doi/10.1021/acsaem.0c00276.

Photovoltaic parameters of the PSCs based on different concentrations of Au−TiO_2 dual ETLs; photovoltaic parameters of the PSCs based on selected ETLs; photovoltaic parameters of the flexible PSCs; schematic of plasmon-induced charge separation; J−V curves of samples based on the configuration of ITO/ETL/Ag; high-resolution TEM characterization; UV−vis transmittance characterization; J−V curves of PSCs based on different concentrations of Au−TiO_2/TiO_2 dual ETLs; J−V curves of PSCs based on selected ETLs; statistical deviation of the photovoltaic parameters of the PSCs based on different concentrations of Au−TiO_2/TiO_2 ETLs; top view SEM characterization; UV−vis absorption characterization; and statistical photovoltaic parameters of flexible PSCs (PDF)

■ AUTHOR INFORMATION

Corresponding Authors

Tung-Chun Lee − *Department of Chemistry and Institute for Materials Discovery, University College London (UCL), London WC1H 0AJ, U.K.*; orcid.org/0000-0002-3163-0000; Email: tungchun.lee@ucl.ac.uk

Da-Qin Yun − *College of Energy, Xiamen University, Xiamen 361005, China*; orcid.org/0000-0003-1667-8417; Email: dqyun@xmu.edu.cn

Authors

Da-Wei Zhao − *College of Energy, Xiamen University, Xiamen 361005, China*

Ming-Yu Yu − *College of Energy, Xiamen University, Xiamen 361005, China*

Ling-Ling Zheng − *College of Energy, Xiamen University, Xiamen 361005, China*; orcid.org/0000-0001-7333-2768

Ming Li − *College of Energy, Xiamen University, Xiamen 361005, China*

Shi-Jie Dai − *College of Energy, Xiamen University, Xiamen 361005, China*

Di-Chun Chen − *Xiamen Branch of Luoyang Ship Material Research Institute, Xiamen 361006, China*

Complete contact information is available at: https://pubs.acs.org/10.1021/acsaem.0c00276

Author Contributions

‖D.-W.Z., M.-Y.Y. and L.-L.Z. contributed equally to this work.

Notes

The authors declare no competing financial interest.

■ ACKNOWLEDGMENTS

This work was supported by the Youth Program of the National Natural Science Foundation of China (no. 61605164), the Development Funds from the College of Energy at Xiamen University (2018NYFZ05), as well as the UCL BEAMS Future Leader Award from the EPSRC 2016 Institutional Sponsorship Award (EP/P511262/1). The EQE

characterization was performed under the assistance of Nanfeng Zheng.

REFERENCES

(1) Li, Z.; Klein, T. R.; Kim, D. H.; Yang, M. J.; Berry, J. J.; van Hest, M. F. A. M.; Zhu, K. Scalable Fabrication of Perovskite Solar Cells. *Nat. Rev. Mater.* **2018**, *3*, 18017.
(2) NREL Research Cell Record Efficiency Chart. https://www.nrel.gov/pv/assets/pdfs/best-research-cell-efficiencies.20190923.pdf (accessed 2019).
(3) Cheacharoen, R.; Rolston, N.; Harwood, D.; Bush, K. A.; Dauskardt, R. H.; McGehee, M. D. Design and Understanding of Encapsulated Perovskite Solar Cells to Withstand Temperature Cycling. *Energy Environ. Sci.* **2018**, *11*, 144−150.
(4) Rong, Y.; Hu, Y.; Mei, A.; Tan, H.; Saidaminov, M. I.; Seok, S. I.; McGehee, M. D.; Sargent, E. H.; Han, H. Challenges for Commercializing Perovskite Solar Cells. *Science* **2018**, *361*, No. eaat8235.
(5) Domanski, K.; Alharbi, E. A.; Hagfeldt, A.; Grätzel, M.; Tress, W. Systematic Investigation of the Impact of Operation Conditions on the Degradation Behaviour of Perovskite Solar Cells. *Nat. Energy* **2018**, *3*, 61−67.
(6) Correa-Baena, J.-P.; Saliba, M.; Buonassisi, T.; Grätzel, M.; Abate, A.; Tress, W.; Hagfeldt, A. Promises and Challenges of Perovskite Solar Cells. *Science* **2017**, *358*, 739−744.
(7) Christians, J. A.; Habisreutinger, S. N.; Berry, J. J.; Luther, J. M. Stability in Perovskite Photovoltaics: A Paradigm for Newfangled Technologies. *ACS Energy Lett.* **2018**, *3*, 2136−2143.
(8) Wang, Z.; Lin, Q. Q.; Chmiel, F. P.; Sakai, N.; Herz, L. M.; Snaith, H. J. Efficient Ambient-Air-Stable Solar Cells with 2D-3D Heterostructured Butylammonium-Caesium-Formamidinium Lead Halide Perovskites. *Nat. Energy* **2017**, *2*, 17135.
(9) Xiao, Z.; Yan, Y. Progress in Theoretical Study of Metal Halide Perovskite Solar Cell Materials. *Adv. Energy Mater.* **2017**, *7*, 1701136.
(10) Zhou, Z.; Pang, S.; Liu, Z.; Xu, H.; Cui, G. Interface Engineering for High-Performance Perovskite Hybrid Solar Cells. *J. Mater. Chem. A* **2015**, *3*, 19205−19217.
(11) Lopez-Varo, P.; Jiménez-Tejada, J. A.; García-Rosell, M.; Ravishankar, S.; Garcia-Belmonte, G.; Bisquert, J.; Almora, O. Device Physics of Hybrid Perovskite Solar Cells: Theory and Experiment. *Adv. Energy Mater.* **2018**, *8*, 1702772.
(12) Christians, J. A.; Schulz, P.; Tinkham, J. S.; Schloemer, T. H.; Harvey, S. P.; Tremolet de Villers, B. J.; Berry, J. J.; Luther, J. M.; Luther, J. M. Tailored interfaces of unencapsulated perovskite solar cells for >1,000 hour operational stability. *Nat. Energy* **2018**, *3*, 68−74.
(13) Yuan, Y.; Huang, J. Ion Migration in Organometal Trihalide Perovskite and Its Impact on Photovoltaic Efficiency and Stability. *Acc. Chem. Res.* **2016**, *49*, 286−293.
(14) Walsh, A.; Stranks, S. D. Taking Control of Ion Transport in Halide Perovskite Solar Cells. *ACS Energy Lett* **2018**, *3*, 1983−1990.
(15) Bag, M.; Renna, L. A.; Adhikari, R. Y.; Karak, S.; Liu, F.; Lahti, P. M.; Russell, T. P.; Tuominen, M. T.; Venkataraman, D. Kinetics of Ion Transport in Perovskite Active Layers and Its Implications for Active Layer Stability. *J. Am. Chem. Soc.* **2015**, *137*, 13130−13137.
(16) Zhou, Y.-Q.; Wu, B.-S.; Lin, G.-H.; Xing, Z.; Li, S.-H.; Deng, L.-L.; Chen, D.-C.; Yun, D.-Q.; Xie, S.-Y. Interfacing Pristine C-60 onto TiO_2 for Viable Flexibility in Perovskite Solar Cells by a Low-Temperature All-Solution Process. *Adv. Energy Mater.* **2018**, *8*, 1800399.
(17) Yang, D.; Yang, R. X.; Wang, K.; Wu, C. C.; Zhu, X. J.; Feng, J. S.; Ren, X. D.; Fang, G. J.; Priya, S.; Liu, S. Z. High Efficiency Planar-Type Perovskite Solar Cells with Negligible Hysteresis Using EDTA-Complexed SnO_2. *Nat. Commun.* **2018**, *9*, 3239.
(18) Arora, N.; Dar, M. I.; Hinderhofer, A.; Pellet, N.; Schreiber, F.; Zakeeruddin, S. M.; Grätzel, M. Perovskite solar cells with CuSCN hole extraction layers yield stabilized efficiencies greater than 20%. *Science* **2017**, *358*, 768−771.
(19) Back, H.; Kim, G.; Kim, J.; Kong, J.; Kim, T. K.; Kang, H.; Kim, H.; Lee, J.; Lee, S.; Lee, K. Achieving Long-Term Stable Perovskite Solar Cells via Ion Neutralization. *Energy Environ. Sci.* **2016**, *9*, 1258−1263.
(20) Chan, K.; Wright, M.; Elumalai, N.; Uddin, A.; Pillai, S. Plasmonics in Organic and Perovskite Solar Cells: Optical and Electrical Effects. *Adv. Opt. Mater.* **2017**, *5*, 1600698.
(21) Clavero, C. Plasmon-Induced Hot-Electron Generation at Nanoparticle/Metal-Oxide Interfaces for Photovoltaic and Photocatalytic Devices. *Nat. Photonics* **2014**, *8*, 95−103.
(22) Ye, M.; Hong, X.; Zhang, F.; Liu, X. Recent Advancements in Perovskite Solar Cells: Flexibility, Stability and Large Scale. *J. Mater. Chem. A* **2016**, *4*, 6755−6771.
(23) Mayer, K. M.; Hafner, J. H. Localized Surface Plasmon Resonance Sensors. *Chem. Rev.* **2011**, *111*, 3828−3857.
(24) Jang, Y. H.; Jang, Y. J.; Kim, S.; Quan, L. N.; Chung, K.; Kim, D. H. Plasmonic Solar Cells: From Rational Design to Mechanism Overview. *Chem. Rev.* **2016**, *116*, 14982−15034.
(25) Zhang, W.; Saliba, M.; Stranks, S. D.; Sun, Y.; Shi, X.; Wiesner, U.; Snaith, H. J. Enhancement of Perovskite-Based Solar Cells Employing Core-Shell Metal Nanoparticles. *Nano Lett.* **2013**, *13*, 4505−4510.
(26) Chandrasekhar, P. S.; Dubey, A.; Reza, K. M.; Hasan, M. D. N.; Bahrami, B.; Komarala, V. K.; Hoefelmeyer, J. D.; He, Q.; Wu, F.; Qiao, H.; Zhang, W.-H.; Qiao, Q. Higher Efficiency Perovskite Solar Cells Using $Au@SiO_2$ Core-Shell Nanoparticles. *Sustainable Energy Fuels* **2018**, *2*, 2260−2267.
(27) Qi, F.; Wang, C.; Cheng, N.; Liu, P.; Xiao, Y.; Li, F.; Sun, X.; Liu, W.; Guo, S.; Zhao, X.-Z. Improving the Performance through SPR Effect by Employing Au@SiO2 Core-Shell Nanoparticles Incorporated TiO_2 Scaffold in Efficient Hole Transport Material Free Perovskite Solar Cells. *Electrochim. Acta* **2018**, *282*, 10−15.
(28) Yuan, Z.; Wu, Z.; Bai, S.; Xia, Z.; Xu, W.; Song, T.; Wu, H.; Xu, L.; Si, J.; Jin, Y.; Sun, B. Hot-Electron Injection in a Sandwiched TiOx-Au-TiOxStructure for High-Performance Planar Perovskite Solar Cells. *Adv. Energy Mater.* **2015**, *5*, 1500038.
(29) Luo, Q.; Zhang, C.; Deng, X.; Zhu, H.; Li, Z.; Wang, Z.; Chen, X.; Huang, S. Plasmonic Effects of Metallic Nanoparticles on Enhancing Performance of Perovskite Solar Cells. *ACS Appl. Mater. Interfaces* **2017**, *9*, 34821−34832.
(30) Fan, R.; Wang, L.; Chen, Y.; Zheng, G.; Li, L.; Li, Z.; Zhou, H. Tailored $Au@TiO_2$ Nanostructures for the Plasmonic Effect in Planar Perovskite Solar Cells. *J. Mater. Chem. A* **2017**, *5*, 12034−12042.
(31) Zhang, C.; Luo, Q.; Shi, J.; Yue, L.; Wang, Z.; Chen, X.; Huang, S. Efficient Perovskite Solar Cells by Combination Use of Au Nanoparticles and Insulating Metal Oxide. *Nanoscale* **2017**, *9*, 2852−2864.
(32) Furube, A.; Du, L.; Hara, K.; Katoh, R.; Tachiya, M. Ultrafast Plasmon-Induced Electron Transfer From Gold Nanodots into TiO_2 Nanoparticles. *J. Am. Chem. Soc.* **2007**, *129*, 14852.
(33) Barbe, C. J.; Arendse, F.; Comte, P.; Jirousek, M.; Lenzmann, F.; Shklover, V.; Gratzel, M. Nanocrystalline Titanium Oxide Electrodes for Photovoltaic Applications. *J. Am. Ceram. Soc.* **1997**, *80*, 3157−3171.
(34) Bastús, N. G.; Comenge, J.; Puntes, V. Kinetically Controlled Seeded Growth Synthesis of Citrate-Stabilized Gold Nanoparticles of up to 200 nm: Size Focusing versus Ostwald Ripening. *Langmuir* **2011**, *27*, 11098−11105.
(35) Yang, W. S.; Noh, J. H.; Jeon, N. J.; Kim, Y. C.; Ryu, S.; Seo, J.; Seok, S. I. High-Performance Photovoltaic Perovskite Layers Fabricated Through Intramolecular Exchange. *Science* **2015**, *348*, 1234−1237.
(36) Eperon, G. E.; Stranks, S. D.; Menelaou, C.; Johnston, M. B.; Herz, L. M.; Snaith, H. J. Formamidinium Lead Trihalide: A Broadly Tunable Perovskite for Efficient Planar Heterojunction Solar Cells. *Energy Environ. Sci.* **2014**, *7*, 982−988.
(37) Kim, H.-S.; Park, N.-G. Parameters AffectingI-VHysteresis of CH3NH3PbI3Perovskite Solar Cells: Effects of Perovskite Crystal

https://dx.doi.org/10.1021/acsaem.0c00276
ACS Appl. Energy Mater. 2020, 3, 9568−9575

Size and Mesoporous TiO2Layer. *J. Phys. Chem. Lett.* **2014**, *5*, 2927−2934.
(38) Liang, Z.; Sun, J.; Jiang, Y.; Jiang, L.; Chen, X. Plasmonic Enhanced Optoelectronic Devices. *Plasmonics* **2014**, *9*, 859−866.
(39) Xiao, Y.; Cheng, N.; Kondamareddy, K. K.; Wang, C.; Liu, P.; Guo, S.; Zhao, X.-Z. W-Doped TiO_2 Mesoporous Electron Transport Layer for Efficient Hole Transport Material Free Perovskite Solar Cells Employing Carbon Counter Electrodes. *J. Power Sources* **2017**, *342*, 489−494.
(40) Xiao, Y.; Wang, C.; Kondamareddy, K. K.; Liu, P.; Qi, F.; Zhang, H.; Guo, S.; Zhao, X.-Z. Enhancing the Performance of Hole-Conductor Free Carbon-Based Perovskite Solar Cells Through Rutile-Phase Passivation of Anatase TiO_2 Scaffold. *J. Power Sources* **2019**, *422*, 138−144.
(41) Zhang, J.; Zhao, B.; Linghui, M.; Hongying, W.; Xudong, W.; Chenxi, L. Controlled Synthesis of Gold Nanospheres and Single Crystals in Hydrogel. *J. Nanopart. Res.* **2007**, *9*, 1167−1171.
(42) Ginsburg, A.; Priel, M.; Barad, H. N.; Keller, D. A.; Borvick, E.; Rietwyk, K.; Kama, A.; Meir, S.; Anderson, A. Y.; Zaban, A. Solid State ITO Vertical Bar Au-NPs Vertical Bar TiO_2 Plasmonic Based Solar Cells. *Sol. Energy Mater. Sol. Cells* **2018**, *179*, 254−259.
(43) Chan, K.; Wright, M.; Elumalai, N.; Uddin, A.; Pillai, S. Plasmonics in Organic and Perovskite Solar Cells: Optical and Electrical Effects. *Adv. Opt. Mater.* **2017**, *5*, 1600698.
(44) Mali, S. S.; Shim, C. S.; Kim, H.; Patil, P. S.; Hong, C. K. In Situ Processed Gold Nanoparticle-Embedded TiO_2 Nanofibers Enabling Plasmonic Perovskite Solar Cells to Exceed 14% Conversion Efficiency. *Nanoscale* **2016**, *8*, 2664−2677.
(45) Yang, D.; Yang, R.; Zhang, J.; Yang, Z.; Liu, S.; Li, C. High Efficiency Flexible Perovskite Solar Cells Using Superior Low Temperature TiO_2. *Energy Environ. Sci.* **2015**, *8*, 3208−3214.
(46) Feng, J.; Yang, Z.; Yang, D.; Ren, X.; Zhu, X.; Jin, Z.; Zi, W.; Wei, Q.; Liu, S. E-Beam Evaporated Nb_2O_5 as An Effective Electron Transport Layer for Large Flexible Perovskite Solar Cells. *Nano Energy* **2017**, *36*, 1−8.

https://dx.doi.org/10.1021/acsaem.0c00276
ACS Appl. Energy Mater. 2020, 3, 9568−9575